CO 2 -to-HCOOH Electrochemical Conversion on Nanostructured Cu x Pd 100–x /Carbon Catalysts

Nihat Ege Şahin, Clément Comminges, Sandrine Arrii, Teko Napporn, Kouakou Kokoh

CO_2-to-HCOOH electrochemical conversion on nanostructured Cu_xPd_{100-x}/C catalysts

Nihat Ege Şahin,[a] Clément Comminges,[a] Sandrine Arrii,[a] Teko W. Napporn,[a] Kouakou B. Kokoh*[a]

Dr. N. E. Şahin, Dr. C. Comminges, Dr. S. Arrii, Dr. T. W. Napporn, Prof. Dr. K. B. Kokoh
Department of Chemistry
IC2MP CNRS UMR 7285, Université de Poitiers
4 rue Michel Brunet - B27, TSA 51106, 86073 Cedex 9 (France)
E-mail: boniface.kokoh@univ-poitiers.fr
ORCID: 0000-0002-5379-7792

Supporting information for this article is given via a link at the end of the document.

Dedication ((This paper is dedicated in memoriam to Prof. Jean-Michel Savéant. His death will be an immense loss within the community of electrochemists to which he greatly contributed to its development))

Abstract: Selective electrochemical conversion of CO_2 to HCOOH is obtained at the surface of a carbon supported bimetallic cathode material composed of copper and palladium nanoparticles. Polycrystalline copper or large copper particles are well-known to catalyze the CO_2 reduction to hydrocarbons at relatively negative potentials, or when their surface is covered by copper oxides (Cu_2O and CuO). Cu-based materials modified by various palladium contents ($0 < x < 100$), were synthesized from micro-wave assisted polyol method to serve as cathode in the selective CO_2-into-HCOOH transformation. Herein, we developed a targeted preparation route toward metal content - catalytic activity relationship correlating atomic ratio with Faradaic efficiency to formate formation (*ca.* 60% FE) at -0.72 V vs. RHE, which represents a 703 mV overpotential at pH=7. Consequently, the occurrence of this reduction reaction slows down the parallel H_2 production from the solvent consumption, while the Cu-Pd neighboring provides an excellent activity and a good efficiency toward CO_2 reduction via the hydridation of the CO_2 molecule to orientate the reaction to formate rather than carbon monoxide or H_2 evolution.

Introduction

Carbon dioxide (CO_2), considered as a major contributor to the greenhouse effect can be valorized as valuable reactant in an electrocatalytic conversion to attractive chemicals.[1-3] Indeed, based on the selectivity of the electrode materials, CO_2 is reducible to hydrocarbons (methane, ethylene),[3-7] syngas (CO, H_2)[8, 9], alcohols such as methanol[10] or ethanol[11] and to formate or formic acid,[9, 12] which is known to be a good candidate as fuel in fuel cell applications. Particularly, formic acid is much more attractive due to its easy storage and transportation as well as its feasible commercialization owing to broad application range. [13] However, high selectivity and Faradaic yield with a reasonable current at low overpotential are far from satisfactory for up-scaling applications. This is because a key challenge concerns the development of effective electrocatalysts that offer selectively catalyzing CO_2 into desired fuels through tunning of morphology. To date, various bulk metal electrodes have been extensively used in the electrochemical CO_2 reduction (CO_2RR). [14] Especially, earth-abundant materials have attracted considerable interest for an efficient CO_2RR because their low-cost is amenable to large-scale use. In this approach, formate was obtained at the surface of transition metals in aqueous medium,[15] while in an aprotic solution (propylene carbonate) the reactant was electro-dimerized to oxalate.[4] The reaction product distribution of the CO_2RR is very sensitive to the applied potential, local pH value and the surface crystal structure of the electrode.[16] As example, copper is well-known to be unique to orientate the CO_2 reduction to hydrocarbons.[17, 18] Both experimental and theoretical investigations unraveled the mechanism behind the selectivity change on Cu(111) and Cu(100) surfaces which facilitate the formations of CH_4 and C_2H_4, respectively.[6] If we exclude the CH_4 formation which involves 8 electrons, and consider herein the CO and HCOOH productions which are 2 electrons reduction products, the electrochemical CO_2RR arises from a compromise between the strength of the interaction between the first intermediate (a one electron reduction product such as adsorbed anion radical $CO_2^{\bullet-}$ or adsorbed hydrogen), the surface structure of the electrode material and subsequent kinetic activation toward protonation or hydridation.[19, 20] The utilization of noble metal electrodes for the CO_2RR mainly leads to CO formation with more or less strong adsorption according its nature (linearly adsorbed CO_L) or (bridge-bonded CO_B).[21, 22] The study of the influence of hydrogen absorption on the catalytic activity of CO_2 reduction toward palladium surfaces unveiled that hydrogen evolution reaction (HER), leading to poor selectivity can be suppressed by hydrogen absorption in the palladium lattice structure and favor another pathway that is short circuiting the adsorbed $CO_2^{\bullet-}$ anion radical formation. The electrochemical behavior of hydrogen has been firstly reported by Hoare et al.[23] They underlined that hydrogen evolution reaction could be
inhibited by hydrogen absorption in the palladium lattice structure, and absorbed hydrogen could promote the yields of CO_2 reduction products by reacting with the adsorbed intermediate species. Additionally, some reports highlighted the role of the palladium lattice

structure on the adsorption and absorption of hydrogen.[24, 25] One can assume that absorbed hydrogen in the Pd lattice may react with reaction intermediates, resulting in increasing the CO_2 reduction efficiency.[24] Recently, palladium is reported to be a cathode that can catalyze formate production with overpotential lower than 200 mV; CO was formed as side product, causing surface poisoning.[26-29] More significantly, cooperation between Pd and Cu materials has recognized especially in CO_2 electrolysis due to their bimetallic capability of promoting formate production with high efficiency at low overpotentials.[30-32] As suggested by Savéant, nanoscaling may change the reaction selectivity.[20] Thus, the example of electrochemical hydridation of CO_2 into $HCOO^-$ *versus* H_2 formation in aqueous media is an ideal example to prove this concept. The reaction mechanism can be summarized in three elementary steps:

1) Volmer step: $AH + e^- \rightarrow H_{ads} + A^-$
2) Heyrovsky step: $H_{ads} + AH + e^- \rightarrow H_2 + A^-$
3) CO_2 reduction: $H_{ads} + CO_2 + e^- \rightarrow HCOO^-$

The common first step is the formation of H_{ads} that is the reductive specie that can lead to the two competitive reactions 2) and 3). In order to favor the CO_2 reduction reaction, one has to slow down the Heyrovsky step, while favoring the CO_2 hydridation reaction that ends up to $HCOO^-$. That can be achieved by both stabilizing the H_{ads} species at the surface of a catalyst and increase the CO_2 diffusion / accessibility to the catalyst surface. This finding opened up a new research perspective targeting the tuning of the adsorbed hydrogen surface coverage on palladium, resulting in an increase in the selectivity for CO_2 reduction.[24] Later on, the particular ability of absorbing hydrogen in Pd crystallographic network was highlighted.[33, 34] In this context, an effective modification of Pd with Cu was reported as reflected by FE for CO production greater than 73 and 86% when the reaction was performed on $Pd_{56}Cu_{44}$/C and $Pd_{85}Cu_{15}$/C, respectively with impractical overpotentials. The hydridation of the CO_2 molecule, by combining Cu nanoparticles with those of Pd for efficiently producing formic acid is the main concern in the present investigation. From this standpoint, nanostructured Cu_xPd_{100-x} cathode materials dispersed in the carbon substrate (Vulcan XC-72R) with a 40 wt.% metal loading were synthesized through microwave-heated polyol process. The impact of electrocatalyst composition on the CO_2 electroreduction activity and selectivity in $NaHCO_3$ electrolyte at room temperature are discussed.

Results and Discussion

Typical EDX spectrum and TEM micrograph of the $Cu_{50}Pd_{50}$/C material with its corresponding mean particle size distribution histogram, based on more than 200 nanoparticles, are depicted in Figure 1. The TEM measurements (Figure S1) confirm that the Cu_xPd_{100-x}/C are well-dispersed on the surface of carbon substrate with a narrow particle size distribution, which shows decrease from 60 to 3.50 nm by co-addition of palladium. This phenomenon may result from the incorporation of Cu in the face-centered cubic (*fcc)* structure of Pd as the atomic radius of Cu (1.45 Å) is smaller than that of Pd (1.69 Å). The EDX spectrums (Figures 1b and S2) provide the characteristic L_α and L_β peaks of copper and palladium, evidencing that the nanoparticles are composed of Cu and Pd elements. The EDX results listed in Table S1 show that the Cu/Pd atomic ratios are close to the expected nominal values, indicating that nanoparticles preparation is highly dependent on the operating conditions of the microwave-heated polyol reduction process.

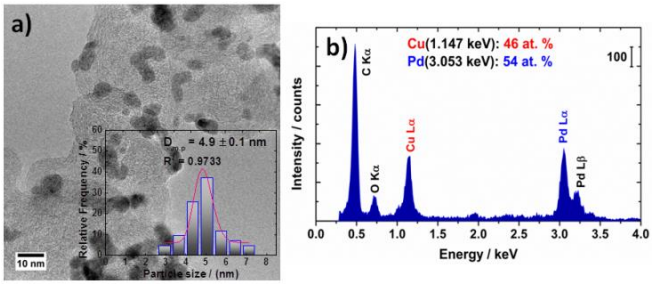

Figure 1. a) TEM micrograph of the $Cu_{50}Pd_{50}$/C material. The inset represents the corresponding mean particle size ($D_{m,p}$) distribution histogram. b) Elemental composition of the catalyst from EDX measurement.

To determine the crystallite size and corresponding lattice parameters, XRD analyses were performed on the as-prepared materials (Figure 2). As indicated in Figure 2a, all the XRD patterns show the main characteristic peaks of the face-centered cubic (*fcc*) crystalline Pd, Cu, and binary Cu/Pd materials. The peak at about 2θ=25º is attributed to graphite (002) crystallographic plane of Vulcan XC-72R carbon support.[35] The peaks at 40.1º, 46.7º, 68.2º, 82.1º and 86.5º correspond, respectively, to the reflection planes (111), (200), (220), (311) and (222) of the Pd *fcc* structure. Similarly, the peaks at 43.2º, 50.3º, 74.1º, 90.0º and 95.1º correspond, respectively to the reflection planes (111), (200), (220), (311) and (222) of the Cu *fcc* structure. Note that the other four peaks centered at 29.5º, 36.3º, 42.3º and 61.3º are characteristic of *fcc* crystallite Cu_2O [36], corresponding to the diffraction peaks of (110), (111), (200) and (220), respectively. The diffraction peaks as to binary Cu/Pd catalysts expose a shift toward higher 2θ values with respect to corresponding peaks in the Pd/C catalysts (Figure 2b), indicating that the synthesis procedure is beneficial for alloying Cu and Pd. This confirms that the lattice parameter of bimetallic CuPd/C catalysts is smaller than bulk Pd (3.8881 Å). Furthermore, according to Vegard`s law [37], the linear relationship between lattice parameter and alloy composition is a clear indication of an alloying behavior. It is the fact to predict that the lattice parameter in Cu/Pd alloy composition increases with the palladium content compared to pure copper, because the

palladium atoms are slightly bigger than those of copper. Consequently, a positive deviation from Cu/C with increasing the Pd content is observed in Vegard's plot (Fig. 2c) and indicating that incorporation of Cu into the Pd lattice is favorable and showing that no segregation effect occurs on the alloys.

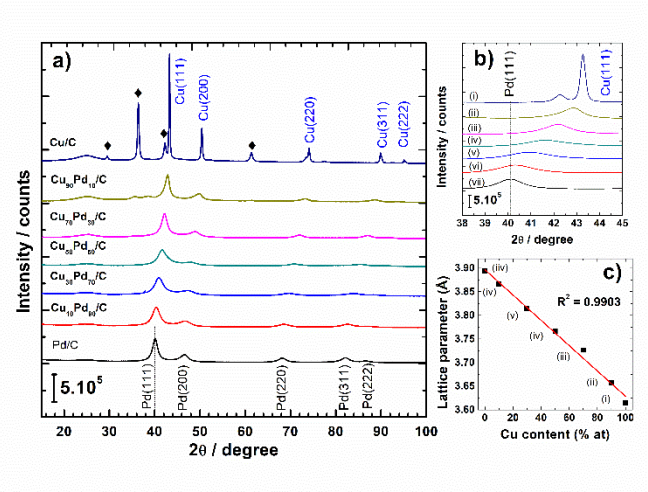

Figure 2. (**a**) XRD patterns of the prepared catalysts, (b) the enlarged XRD patterns of the (111) crystalline faces that correspond to (i) Cu/C, (ii) $Cu_{90}Pd_{10}$/C, (iii) $Cu_{70}Pd_{30}$/C, (iv) $Cu_{50}Pd_{50}$/C, (v) $Cu_{30}Pd_{70}$/C, (vi) $Cu_{10}Pd_{90}$/C and (vii) Pd/C. (c) Vegard`s plot presenting the *fcc* lattice constant (a_{111}) of the atomic composition of Cu in Cu/Pd alloys.

Figure 3 shows the cyclic voltammograms (CVs) of the different prepared Cu_xPd_{100-x}/C electrodes recorded in the potential range -1.0 - 1.5 V vs. RHE. Although this study is related to CO_2 reduction, it appears useful to record the CVs including the oxidation potential domain to give additional evidence to the presence of both metals (Cu and Pd) in the bimetallic catalyst. When the CV was recorded up to this upper potential limit, the Cu and Pd surface oxidations can be observed during the forward potential scan (see also Figure S3). And during the backward scan these oxide reductions are evidenced from 0.90 to 0.20 V. It can be noticed in Figure S3 the redox couples a_1/c_1 and a_2/c_2 attributed to Cu/Cu_2O and Cu_2O/CuO, respectively, whereas the redox couple a_3/c_3 is related to Pd/PdO species. Moreover, a broad CO_2-electroreduction peak (c_4) is observed in the presence of CO_2. For the present concern, the CO_2RR starts from ca. -0.13 V *versus* RHE on Cu/C and 130 mV earlier at the surface of the bimetallic $Cu_{50}Pd_{50}$/C cathode (Figure 3). On bimetallic cathodes CuPd, a similar trend was observed by S. Ma et al.[18] When the reduction process is performed at more cathodic potentials, the dominance of hydrogen evolution reaction (c_5, HER) over CO_2 electroreduction, arises from the electrolyte reduction.

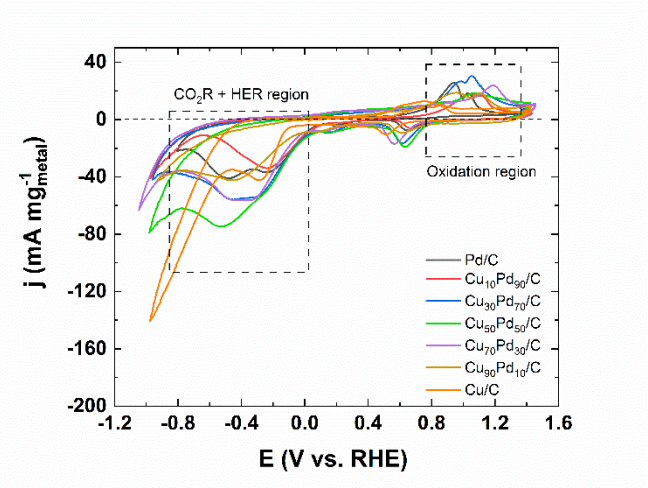

Figure 3. Cyclic voltammograms of Cu/C and Cu_xPd_{100-x}/C electrode materials at 50 mV s^{-1} in a 0.5 mol L^{-1} $NaHCO_3$ electrolytic solution at 25 °C in the presence of CO_2.

As can be seen in the cyclic voltammograms, during the cathodic scan, hydrogen adsorption/absorption phenomena (between 0.35 and 0.0 V vs. RHE) occurs, followed by the hydrogen evolution. Comparing the CVs recorded in the absence of CO_2 (black curves in Fig. S3), one can notice the dependence of the shape of hydrogen desorption region (hydrogen oxidation region, between 0.0 and 0.60 V vs. RHE, Fig. S3b, peak a4), on the palladium content during the anodic scan. The early studies on CO_2 electroreduction

demonstrated that the electrocatalytic activity strongly depends on the size and composition of the metal nanoparticles.[38, 39] In a recent investigation, it was demonstrated from calculations based on statistical cuboctahedron cluster model that in the size range of interest of this study (3-6 nm) the H_{ads}/Pd ratio is heavily evolving. The most favorable adsorption sites for hydrogen on Pd are 3-fold *hcp* (dominant on small crystallite size), 3-fold *fcc* (dominant for large crystallites) and hollow 4-fold sites on faces (100 and 111). The ratio of these sites depends directly on the crystallite size. The consequence is that in the size range less than about 7.5 nm, the H/Pd ratio rapidly increases as the particle size decreases. For cuboctahedral Pd particles, the H_{ads}/Pd ratio is 0.19 for a 6.5 nm particle whereas it is almost doubled on a 3.5 nm particle (H_{ads}/Pd = 0.34).[40] This indicates that smaller particles will favor higher hydrogen surface coverage. Moreover, the main difference between pure Cu and pure Pd catalysts is that in the case of pure Pd, a reversible hydrogen cathodic adsorption /anodic desorption peak (c_4/a_4 in Fig. S3b) is observed in the absence of CO_2, whereas it is irreversible in the case of Cu. In CO_2 saturated electrolyte, the a_4 desorption peak observed on Pd vanishes, what is the indication that adsorbed hydrogen actively participates to the CO2RR on Pd electrode. Conversely, the c_4 peak observed on Cu electrode is mostly due to HER with a small amount of formate as recently reported.[41] This indication tends to the conclusion that HER is inhibited on Pd containing catalysts. This is consistent with the suggested mechanism related to the formate formation via adsorbed hydrogen. Herein, it was found that $Cu_{50}Pd_{50}$/C (Fig. 3) exhibits the highest cathodic current density in this cathodic region, (j = -74.5 mA mg^{-1} at the peak potential), suggesting that this catalyst composition might be the most efficient for CO2RR. This is an evidence that the Heyrovsky step rate constant is considerably decreased, while the CO_2RR rate constant is not affected. In addition, the contribution of the possibly reduced CO_2 intermediates (such as CO_{ad} and $COOH_{ad}$) being adsorbed at the electrode surface may lead to blocking of the hydrogen region, and consequently, a shift of the oxidation species towards more positive values (in the range 0.75 - 1.35 V vs. RHE), as depicted in Fig. 3. In light of the products obtained, and considering the adsorbates involved in the reaction mechanisms, one could expect that any species involved in the reduction would be determined through a specific peak in the oxidation zone (Figure 3). Accordingly, CO stripping experiments were performed (Figure S4); depending on the composition of the Pd and Cu based electrode, the CO oxidation range is so large that any prediction becomes difficult.

In a previous work on copper electrodes, it was observed that the conversion of CO_2 to formic acid was obtained at an optimal potential of -0.72 V vs. RHE.[41] In the present study, electrolysis of 2.0 bar CO_2 was first performed at different electrode potentials and an optimum HCOOH production was also observed at -0.72 V vs RHE for the $Cu_{50}Pd_{50}$/C electrode (Fig. 5b). Therefore, this potential was chosen for CO_2 reduction on all prepared electrodes. To compare their activity, all the electrode materials were prepared with the same metal loading (1.9 mg cm^{-2}) deposited onto carbon Toray used as conducting substrate; each electrolysis was stopped when a coulombic charge comprised between 50 and 120 C (Q) was achieved. As can be observed in Figure 4, the profile of the current density strongly depends on the cathode composition, indicating a good stability for $Cu_{10}Pd_{90}$/C and $Cu_{50}Pd_{50}$/C toward the CO2RR.

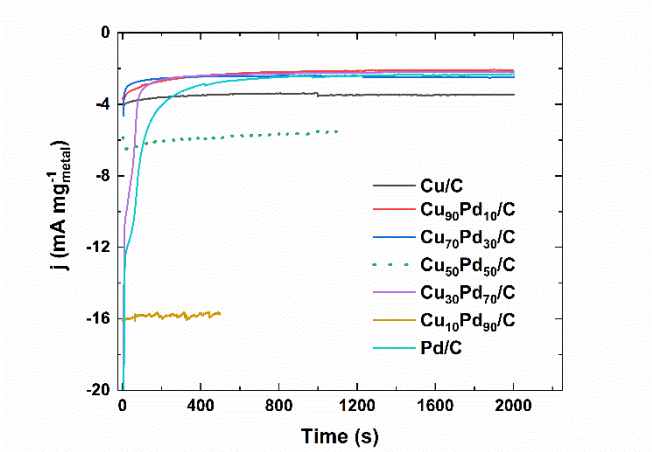

Figure 4. Chronoamperometry curves of CO_2 electroreduction on Cu_xPd_{100-x}/C at -0.72 V vs. RHE in a 0.5 mol L^{-1} $NaHCO_3$ electrolytic solution.

Figure 5a illustrates the Faradaic efficiencies (FEs) for generating formate depending on Cu atomic content in a 0.5 mol L^{-1} $NaHCO_3$ solution. The CO_2 electrochemical reduction leads to CO and formate, H_2 production being a parallel reduction of the solvent because overpotential of CO_2 activation overlaps with that of the solvent. With alloying Cu with Pd gradually, the trends in FEs for formate, CO and H_2 change evidently on the prepared electrode surfaces. The optimum Faradaic yield toward production of formate of 59.5% could be served a synergistic effect in bimetallic $Cu_{50}Pd_{50}$/C nanoparticles that provide more effectiveness towards electrochemical reduction of CO_2. The FE of the CO production rises to 17% on Pd/C, while it is ca. 4 folds lower on Cu/C at the same applied electrode potential. On the other hand, FE of CO is decreasing to 1% on $Cu_{50}Pd_{50}$/C, which suggests that the ratio (1:1) of the CuPd bimetallic composition is favorable to the CO_2 to HCOOH conversion (Figure 5). To further investigate the catalytic activities for electro-reducing CO_2, the selectivity evolution is also observed with the electrode potential for $Cu_{50}Pd_{50}$/C ranging from -0.39 to -1.09 V vs. RHE. As can be seen in Figure 5b, the Faradaic efficiency for formate typically increases with the applied potential from -0.39 V (26.4%) and reached an optimum value of 59.5 % up to -0.72 V without sacrificing the CO_2 reduction reaction activity. As expected, the FE for formate production is significantly higher than that for hydrogen, strongly confirming the role of palladium on uniquely absorbing hydrogen in its lattice structure as well as keeping an adequate H_{ads} surface coverage. Min et al. showed that the CO_2 to HCOOH reduction starts on Pd/C

without overpotential. [27] Although no electrolysis was performed at ca. -0.017 V vs. RHE (at pH=7), the shape of the FE_{HCOOH} curve tends to confirm this production in the region of the equilibrium potential, where the electrode is particularly covered with $H_{ads/abs}$. Nevertheless, Figure 5 shows that at -0.72 V vs. RHE (η = 703 mV) an optimal production of formate occurs on $Cu_{50}Pd_{50}$/C having the ratio H_{ads} / CO_{2ads} favorable to its formation. For some compositions of the cathode catalyst, the mass balance fluctuates either with the quantification of H_2 or due to undetermined products in the gas phase. Figure 5 illustrates this very well since it is at one of these compositions that the HCOOH concentration is high and at the same time the mass balance is far from 100%.

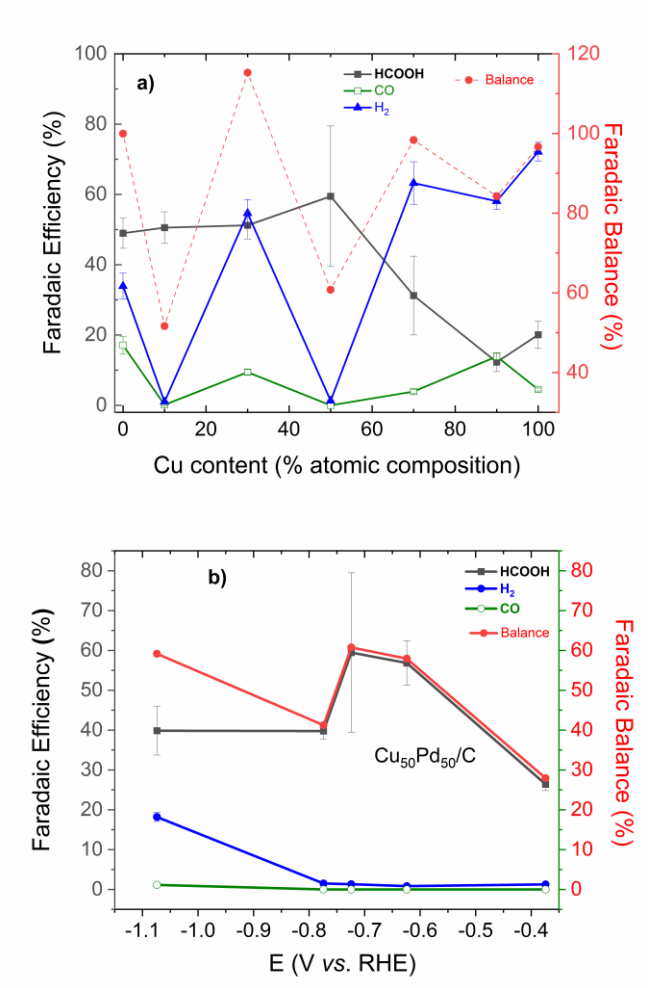

Figure 5. Variation in the Faradaic efficiency (F.E) of the reaction products and mass balance **a)** on Cu_xPd_{100-x}/C as function of the Cu content and at -0.72 V vs. RHE. **b)** on $Cu_{50}Pd_{50}$/C as function of the electrode potential in CO_2 (2.0 bar) 0.5 mol L^{-1} $NaHCO_3$. For H_2 and CO, error bars were calculated from a Student analysis with a confidence interval of 95% based on 8 µ-GC injections. For HCOOH, error bars were calculated from a standard deviation analysis on 3 HPLC injections.

The rapid production rate of formate on the bimetallic composition $Cu_{50}Pd_{50}$/C (Figure S5) can be explained by an optimization of the H_{ads}/CO_{2ads} ratio on this cathode. Indeed, the particle size (4.9 nm) and the Cu/Pd ratio (Figure 1) could be favorably related to the proximity of the adsorbates involved and even accelerate the formation of $HCOO^-$, as stated in the literature. [20, 40] The addition of copper to palladium has a direct influence on the H_{ads} surface coverage but also on the H_{ads} to H_{ads} distance. This is also in the favor of CO_2 diffusion and adsorption on the electrocatalyst surface, giving as a direct consequence and optimal ratio of H_{ads} / CO_{2ads} that can suppress the Heyrovsky step and improve the CO2RR rate constant. This selective transformation shows that the combination of copper and palladium particles in the bimetallic composition is also helpful to decrease the CO formation and at the same time to facilitate the hydridation of CO_2 adsorbate to formate. The optimal atomic ratio appears at $Cu_{50}Pd_{50}$/C, in which the highest FE for formate production reaches up to 60% at -0.72 V vs. RHE. Thus, $Cu_{50}Pd_{50}$/C binary alloy catalyst may provide an effective cathode catalyst to drive the energy conversion devices.

Conclusions

In summary, we demonstrate herein that valorization of CO_2 can be implemented through its electrochemical conversion to formate, which is a promising fuel for fuel cell application. Judicious combination of electro)analytical techniques allow the unambiguous determination of the reaction product over different Cu_xPd_{100-x}/C cathodes prepared from micro-wave assisted polyol method. Formate occurrence strongly depends on the particles size distribution and the Pd content in the bimetallic CuPd composition. About 60% of selectivity towards this molecule is obtained at -0.72 V vs. RHE; this reveals that in this potential domain low H_2 and CO are produced in the benefit of adsorbed CO_2 and proton (H_{ads}) combining to provide $HCOO^-$ determined as the principal product of the CO_2 reduction reaction at the $Cu_{50}Pd_{50}$/C surface.

Experimental Section

Electrocatalysts synthesis: The Cu_xPd_{100-x} nanocatalysts used for the CO_2 electrochemical reduction were prepared from polyol method assisted by micro-wave irradiation [42] and their compositions were tuned by the atomic ratios (Cu^{2+}/Pd^{2+} = 100:0, 90:10, 70:30, 50:50, 30:70, 10:90, 0:100, respectively) of the metal precursors. They were dispersed in carbon black (Vulcan XC 72R, Cabot), as support and to target a metal loading of 40 wt.%. Basically, metal precursors ($CuCl_2$, Alfa Aesar and K_2PdCl_4, Alfa Aesar) with different atomic ratios were dissolved in 100 mL diethylene glycol (DEG, Alfa Aesar) that acts both as a solvent and a reducing agent under 30 min stirring at 25 °C. The pH value was adjusted at 11 with 2.0 mol L^{-1} NaOH in DEG prior to add the desired amount of carbon substrate (Vulcan XC72R), which is previously treated under N_2 atmosphere at 400 °C for 4 h. The mixture was then maintained under vigorous stirring (1000 rpm) for 15 min in order to have a homogeneous suspension. Afterwards the mixture was rapidly heated in the microwave oven (CEM, Synthesis Technology Inside) with the power output of 1600W irradiation at 185°C under N_2 gas flowing (1.0 bar) for 30 min. Finally, the mixture was filtered on a 0.22 µm GSWP (Fisher-Bioblock paper) and washed several times with ultra-pure water (18.2 MΩ cm, 20 °C). The remaining material (Cu_xPd_{100-x}/C) was then dried in an oven at 70 °C for 12 h.

Physicochemical characterization: The obtained nanomaterials were physicochemically characterized using various tools. X-ray diffraction (XRD) data were collected in the 2θ range of 15-100 º with steps of 0.05 º and fixed acquisition time of 2 min $step^{-1}$ using an ENPYREAN (PANalytical) diffractometer in Bragg-Brentano θ-θ configuration with a copper tube powdered at 45 kV and 40 mA. The crystallite size of the prepared catalysts was determined from the Scherrer equation.[35, 43] The lattice parameter was evaluated by using Bragg`s law [44] to be combined by interplanar spacing of the crystallographic plane (*hkl*). The relationship between the catalyst compositions and their crystal lattice parameter was determined by Vegard`s law.[45, 46] The related parameters of the crystalline phases were calculated using Fityk free software and listed in Table S1. Morphology and particles size dispersion were evaluated by using high resolution transmission electron microscopy (HR-TEM; using a TEM/STEM JEOL 2100 UHR microscope at 200 kV accelerating voltage with LaB_6 emitter. The point and linear resolution were 0.19 nm 0.14 nm, respectively. The elemental analysis was performed using TEM coupled energy dispersive X-ray (EDX) spectroscopy (JED Series AnalysisProgram, JEOL) with a LaB6 filament and CCD camera (Gatan Ultrascan 2Kx2K) attached to the microscope.

Cyclic voltammetry and CO stripping measurements: Cyclic voltammetry and CO striping measurements were carried out with a rotating disk electrode (RDE, with a 5 mm diameter) in a thermo-stated three-electrode electrochemical cell using Ag|AgCl (sat. KCl) and glassy carbon slab as reference and counter electrodes, respectively. Prior to each electrochemical measurement, the RDE was polished with three different grades of alumina slurry (1.0 µm, 0.5 µm and 0.05 µm) on a synthetic cloth, then rinsed with ultra-pure water and ultrasonicated in water/ethanol (50:50, v/v) for 5 min. The catalytic ink was prepared by ultrasonically dispersing 5 mg of catalytic powder in a homogeneous mixture composed of a 50 µL Nafion® solution (5 wt.% from Sigma Aldrich) and 450 µL of ultra-pure water. After homogenization, 10 µL of the ink was deposited from micro syringe onto a fresh polished glassy carbon (yielding a 0.204 mg cm^{-2} metal loading) for each CV and CO stripping measurements. The solvent was then evaporated in a stream of ultra-pure nitrogen at room temperature. All the CV and CO stripping experiments were performed at room temperature using 0.5 mol L^{-1} $NaHCO_3$. Before each experiment, the electrolyte was deoxygenated by bubbling nitrogen during 30 min. All the potentials were converted into reversible hydrogen electrode (RHE) scale, considering at pH 7 the standard electrode potential of the $CO_2/HCOO^-$ couple, according to Y. Hori: [47]

$CO_{2(g)} + H_2O + 2e^- \leftrightarrow HCOO^- + OH^-$ with E^o= -0.43 V/SHE Eq. 1

which is expressed in RHE scale:

$E_{RHE}(V) = E^o(V_{SHE}, -0.43) + (0.0591 \times pH) = -0.017\ V\ vs.RHE$ Eq.2

As example, the conversion of the potential set at -1.35V vs. Ag|AgCl, KCl sat., RHE was calculated as followed:

$E_{RHE}(V) = E^o(V_{Ag|AgCl}, 0.197) + E_{app.}(V, -1.35) + (0.0591 \times pH)$ Eq. 3

CO_2 reduction electrolysis and product analysis: The CO_2 electrolysis measurements were conducted in a typical H-type electrochemical cell equipped by a bi-potentiostat (AUTOLAB-PGSTAT302N) with Ag|AgCl, KCl sat. reference electrode described elsewhere.[48] As CO_2 and CO can interact with both Cu and Pd, we consider that it is not accurate to take into account only Pd in the calculation of the electrode active surface. Therefore, in cyclic voltammetry and electrolysis experiments, the current densities were normalized with the metal loading (CuPd) deposited on the conducting substrate. For the preparation of Toray carbon paper supported working electrode, 30 mg of as-prepared catalysts were suspended in a 1.5 mL mixture solution of ultra-pure water and 5 wt.% Nafion suspension with a volume ratio of 0.90:0.10. After ultra-sonication for 30 min, the required amount of catalytic ink was dropped on to the Toray carbon paper and dried at room temperature. The catalyst (Cu_xPd_{100-x}/C) loading deposited onto the Toray carbon paper was 4.76 $mg_{cat.}$ cm^{-2} containing a metal loading of 1.90 mg cm^{-2}. Thermal and chemical treatments were avoided to not alter the inherent structure of the electrode materials. The anode and cathode compartments were separated through a Nafion®-117 ion exchange membrane and the cell were designed to have a large electrolyte volume of 100 mL in each compartment, along with a gas headspace of approximately 65 mL above on each side. Prior to use the Nafion®-117 ion exchange membrane, it was pretreated for 8 h at 90 °C in 0.5 mol L^{-1} H_2SO_4 aqueous solution and then rinsed with ultra-pure water several times. The $NaHCO_3$ aqueous solution (0.5 mol L^{-1}, pH 8.15) was used as electrolyte. Prior to CO_2 electrolysis, the electrolyte was firstly deoxygenated by bubbling nitrogen (N_2, pH 8.71) for 30 minutes and just after the catholyte was saturated by CO_2 (pH 7.26) under continuous stirring for 30 min. Then, potentiostatic electrochemical reduction of CO_2 was performed under 2.0 bar of CO_2 saturated conditions. The distance between the working electrode and the counter electrode (Pt/IrO_2) was about 9.0 cm and the effective geometric area of the working electrode was 6.3 cm^2. The gaseous products were collected using micro gas chromatography (Agilent Technologies, 490 µ-GC), which is equipped with a thermal conductivity

detector (TCD) that allows to analyze (i) the permanent gases H_2, N_2 on a Molsieve 5A PoraBond column (ii) the presence of hydrocarbons (methane and ethylene), if produced, on a PoraPlot Q column and (iii) CO and the reactant CO_2 on a COX 1 m HI-BF column. The column temperatures were 80, 60, and 120 °C, respectively, with a constant injection temperature of 100 °C. Helium and Argon were used as the internal carrier standards. The liquid phase was analyzed at the end of the reduction process with a high-performance liquid chromatography (HPLC, including Aminex® HPX-87H Ion Exclusion Column, Dionex Ultimate 3000 Pump, ASI-100 Automated Sample Injector, UV-detector at 210 nm), which permits to determine solely formate. An aqueous solution of sulfuric acid (3.3 mmol L^{-1} H_2SO_4) was used as mobile phase at a 0.60 mL min^{-1} flow rate.

Acknowledgements

This work was financially supported by the European Union (ERDF) and “Région Nouvelle-Aquitaine”. N. E. S. is grateful for Post-doctoral research grant acknowledged by Centre National Scientific Research, France (CNRS, ANR E-CLOCK Project).

The authors declare no competing financial interest.

Keywords: • Carbon dioxide reduction • Palladium-Copper nanoparticles • Formate • Formic acid • Microwave synthesis

[1] K. P. Kuhl, T. Hatsukade, E. R. Cave, D. N. Abram, J. Kibsgaard, T. F. *Jaramillo*, *J Am Chem Soc* **2014**, *136*, 14107-14113.
[2] K. P. Kuhl, E. R. Cave, D. N. Abram, T. F. Jaramillo, *Energy Environ. Sci.* **2012**, *5*, 7050-7059.
[3] R. Kortlever, J. Shen, K. J. P. Schouten, F. Calle-Vallejo, M. T. M. *Koper*, *J. Phys. Chem. Lett.* **2015**, *6*, 4073-4082.
[4] J. Qiao, Y. Liu, F. Hong, J. Zhang, *Chem.Soc. Rev.* **2014**, *43*, 631-675.
[5] P. Friebe, P. Bogdanoff, N. Alonso-Vante, H. Tributsch, *J. Catal*. **1997**, 168, 374-385.
[6] Q. Li, W. Zhu, J. Fu, H. Zhang, G. Wu, S. Sun, *Nano Energy* **2016**, *24*, 1-9.
[7] Q. Zhu, X. Sun, D. Yang, J. Ma, X. Kang, L. Zheng, J. Zhang, Z. Wu, B. Han, *Nat Commun* **2019**, 10, 3851.
[8] J. L. DiMeglio, J. Rosenthal, *J. Am. Chem. Soc.* **2013**, 135, 8798-8801.
[9] S. Subramanian, E. C. Duin, S. E. J. Fawcett, F. A. Armstrong, J. Meyer, M. K. Johnson, *J Am Chem Soc* **2015**, 137, 4567-4580.
[10] J. Albo, M. Alvarez-Guerra, P. Castano, A. Irabien, *Green Chem.* **2015**, *17*, 2304-2324.
[11] N. Theaker, J. M. Strain, B. Kumar, J. P. Brian, S. Kumari, J. M. Spurgeon, *Electrochim Acta* **2018**, 274, 1-8.
[12] X. Lu, D. Y. C. Leung, H. Wang, M. K. H. Leung, J. Xuan, *ChemElectroChem* **2014**, 1, 836-849.
[13] A. S. Agarwal, Y. Zhai, D. Hill, N. Sridhar, *ChemSusChem* **2011**, 4, 1301-1310.
[14] Y. Wang, J. Liu, Y. Wang, A. M. Al-Enizi, G. Zheng, *Small* **2017**, 13, 1701809.
[15] R. P. S. Chaplin, A. A. Wragg, *J. Appl. Electrochem*. **2003**, 33, 1107-1123.
[16] Z. Zhang, L. Melo, R. P. Jansonius, F. Habibzadeh, E. R. Grant, C. P. Berlinguette, *ACS Energy Lett*. **2020**, 3101-3107.
[17] H. Mistry, A. S. Varela, S. Kühl, P. Strasser, B. R. Cuenya, *Nat. Rev. Mater.* **2016**, 1, 16009.
[18] S. Ma, M. Sadakiyo, M. Heima, R. Luo, R. T. Haasch, J. I. Gold, M. Yamauchi, P. J. A. Kenis, *J Am Chem Soc* **2017**, 139, 47-50.
[19] S. Zhang, P. Kang, T. J. Meyer, *J. Am. Chem. Soc*. **2014**, 136, 1734-1737.
[20] J.-M. Saveant, *ChemElectroChem* **2016**, 3, 1967-1977.
[21] B. Beden, A. Bewick, K. Kunimatsu, C. Lamy, *J. Electroanal. Chem. Interfacial Electrochem.* **1982**, 142, 345-356.
[22] C. Zhu, J. Zeng, J. Tao, M. C. Johnson, I. Schmidt-Krey, L. Blubaugh, Y. Zhu, Z. Gu, Y. Xia, *J Am Chem Soc* **2012**, 134, 15822-15831.
[23] J. P. Hoare, S. Schuldiner, *J. Electrochem Soc*. **1955**, *102*, 485-489
[24] K. Ohkawa, K. Hashimoto, A. Fujishima, Y. Noguchi, S. Nakayama, *J. Electroanal. Chem.* **1993**, 345, 445-456.
[25] A. Zalineeva, S. Baranton, C. Coutanceau, G. Jerkiewicz, *Science Adv*. **2017**, *3*, e1600542.
[26] D. Gao, H. Zhou, F. Cai, J. Wang, G. Wang, X. Bao, *ACS Catal.* **2018**, *8*, 1510-1519
[27] X. Min, M. W. Kanan, *J Am Chem Soc*. **2015**, *137*, 4701-4708
[28] S. Pérez-Rodríguez, N. Rillo, M. J. Lázaro, E. Pastor *Appl. Catal. B: Environ.* **2015**, *163*, 83-95
[29] B. Endrődi, G. Bencsik, F. Darvas, R. Jones, K. Rajeshwar, C. Janáky *Prog. Energy Combust. Sci.*, **2017**, *62*, 133-154.
[30] X. Liu, L. Zhu, H. Wang, G. He, Z. Bian *RSC Adv.* **2016**, *6*, 38380-38387
[31] M. Li, J. Wang, P. Li, K. Chang, C. Li, T. Wang, B. Jiang, H. Zhang, H. Liu, Y. Yamauchi, N. Umezawa, J. Ye *J. Mater. Chem. A*. **2016**, *4*, 4776-4782.
[32] K. Ohkawa, Y. Noguchi, S. Nakayama, K. Hashimoto, A. Fujishima *J. Electroanal. Chem.* **1993**, *348*, 459-464.
[33] Y. Holade, C. Canaff, S. Poulin, T. W. Napporn, K. Servat, K. B. Kokoh, *RSC Adv.* **2016**, 6, 12627-12637.
[34] Y. Soldo-Olivier, E. Sibert, B. Previdello, M. C. Lafouresse, F. Maillard, M. De Santis, *Electrochim. Acta* **2013**, 112, 905-912.
[35] Y. Holade, C. Morais, K. Servat, T. W. Napporn, K. B. Kokoh, *Phys. Chem. Chem. Phys*. **2014**, 16, 25609-25620.
[36] D. Ren, Y. Deng, A. D. Handoko, C. S. Chen, S. Malkhandi, B. S. Yeo, *ACS Catal.* **2015**, 5, 2814-2821.
[37] S. Biswas, S. Kar, S. Santra, Y. Jompol, M. Arif, S. I. Khondaker, *J. Phys. Chem. C* **2009**, 113, 3617-3624.
[38] R. J. Gilliam, D. W. Kirk, S. J. Thorpe, *Electrochem. Commun*. **2007**, 9, 2276-2279.
[39] R. Reske, H. Mistry, F. Behafarid, B. Roldan Cuenya, P. Strasser, *J Am Chem Soc* **2014**, 136, 6978-6986.
[40] F. Drault, C. Comminges, F. Can, L. Pirault-Roy, F. Epron, A. Le Valant *Materials*. **2018**, *11*, 819.
[41] N. E. Şahin, C. Comminges, A. Le Valant, J. Kiener, J. Parmentier, T. W. Napporn, G. Melinte, O. Ersen, K. B. Kokoh, *ChemPhysChem*. **2018**, *19*, 1371-1381
[42] N. E. Sahin, T. W. Napporn, L. Dubau, F. Kadirgan, J.-M. Léger, K. B. Kokoh, *Appl. Catal. B: Environ*. **2017**, 203, 72-84.
[43] S. Beyhan, J.-M. Léger, F. Kadırgan, *Appl. Catal. B: Environ*. **2013**, 130–131, 305-313.
[44] M. F. Perutz, *Nature* **1971**, 233, 74-76.
[45] M. J. Lambregts, S. Frank, *Talanta* **2004**, 62, 627-630.
[46] L. Zhang, S. Li, *Physica B: Condensed Matter* **2014**, 434, 38-43.
[47] Y. Hori, in *Electrochemical CO2 Reduction on Metal Electrodes,* (Eds.: C. Vayenas, et. al.), Springer, New York, **2008**, Chap. 3, pp.89-189.
[48] N. Sahin, W. O. Silva, M. R. Camilo, E. A. Ticianelli, F. H. B. Lima, J. Parmentier, C. Comminges, T. W. Napporn, K. B. Kokoh, *Sustain. Energy Fuels* **2020**, 4, 6045-6053.

Selective CO_2-to-HCOOH conversion occurred at the surface carbon supported Cu_xPd_{100-x} nanoparticles. Higher Faradaic efficiency (*ca*. 60%) was obtained on $Cu_{50}Pd_{50}$/C at -0.72 V vs. RHE, where low parallel H_2 and CO production occurs.

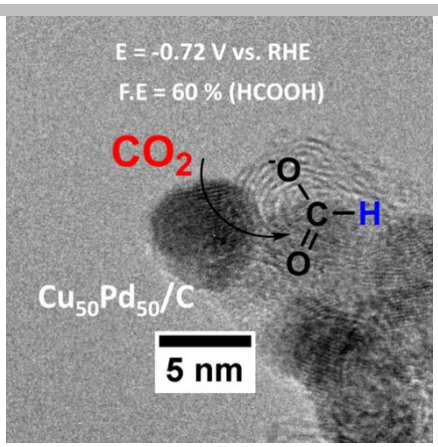

Nihat Ege Şahin,[a] Clément Comminges,[a] Sandrine Arrii,[a] Teko W. Napporn,[a] Kouakou B. Kokoh[a]*

Page No. – Page No.

CO_2-to-HCOOH electrochemical conversion on nanostructured Cu_xPd_{100-x}/C catalysts

Supporting Information

CO_2-to-HCOOH electrochemical conversion on nanostructured Cu_xPd_{100-x}/C catalysts

Nihat Ege Şahin,[a] Clément Comminges,[a] Sandrine Arrii,[a] Teko W. Napporn,[a] Kouakou B. Kokoh*[a]

Table S1. Physico-chemical characterization parameters of the as-prepared electrocatalysts. Atomic composition, mean particle size, lattice parameter and average crystallite size were assessed from powder from EDX, TEM and XRD, respectively.

Electrocatalyst (μ-wave heated polyol method)	**Nominal composition [at. %]**	**Atomic composition (EDS) [at. %]**	**Mean particle size (TEM) (nm)**	**Lattice parameter (XRD) [Å]**	**Average crystallite size (XRD) (nm)**
Cu/C	100	-	~ 60.0	3.6175	69.9
$Cu_{90}Pd_{10}$/C	90 : 10	89 : 11	6.3 ± 0.5	3.6497	4.2
$Cu_{70}Pd_{30}$/C	70 : 30	69 : 31	6.1 ± 0.3	3.7060	5.7
$Cu_{50}Pd_{50}$/C	50 : 50	46 : 54	4.9 ± 0.1	3.7518	4.3
$Cu_{30}Pd_{70}$/C	30 : 70	29 : 71	4.4 ± 0.2	3.8093	4.3
$Cu_{10}Pd_{90}$/C	10 : 90	11 : 89	4.4 ± 0.3	3.8666	4.8
Pd/C	100	-	3.5 ± 0.1	3.8881	6.6

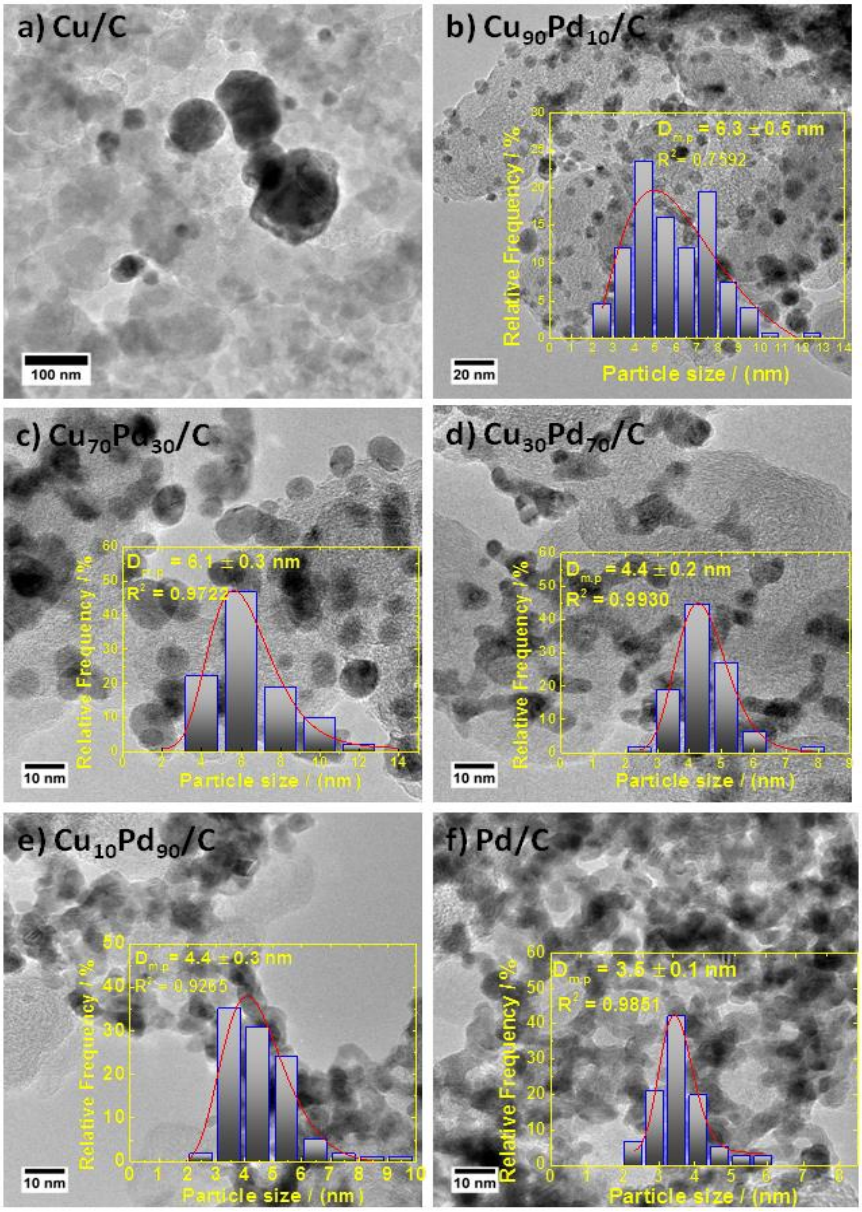

Figure S1. TEM micrographs of a) Cu/C, b) $Cu_{90}Pd_{10}$/C, c) $Cu_{70}Pd_{30}$/C, d) $Cu_{30}Pd_{70}$/C, e) $Cu_{10}Pd_{90}$/C, f) Pd/C with the corresponding mean particle size ($D_{m.p}$) distribution histograms. The mean particle size was evaluated by considering the most representative particle numbers and fitting the histogram using LogNormal function.

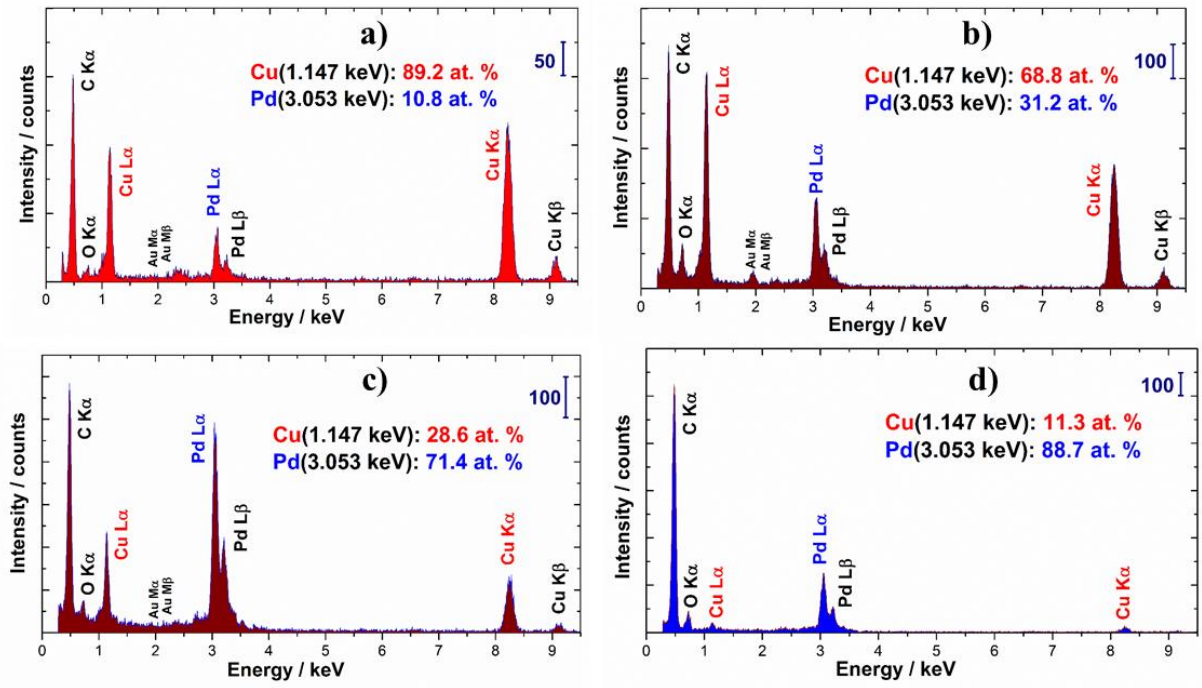

Figure S2. TEM-EDX micrographs of a) $Cu_{90}Pd_{10}$/C, b) $Cu_{70}Pd_{30}$/C, c) $Cu_{30}Pd_{70}$/C, d) $Cu_{10}Pd_{90}$/C.

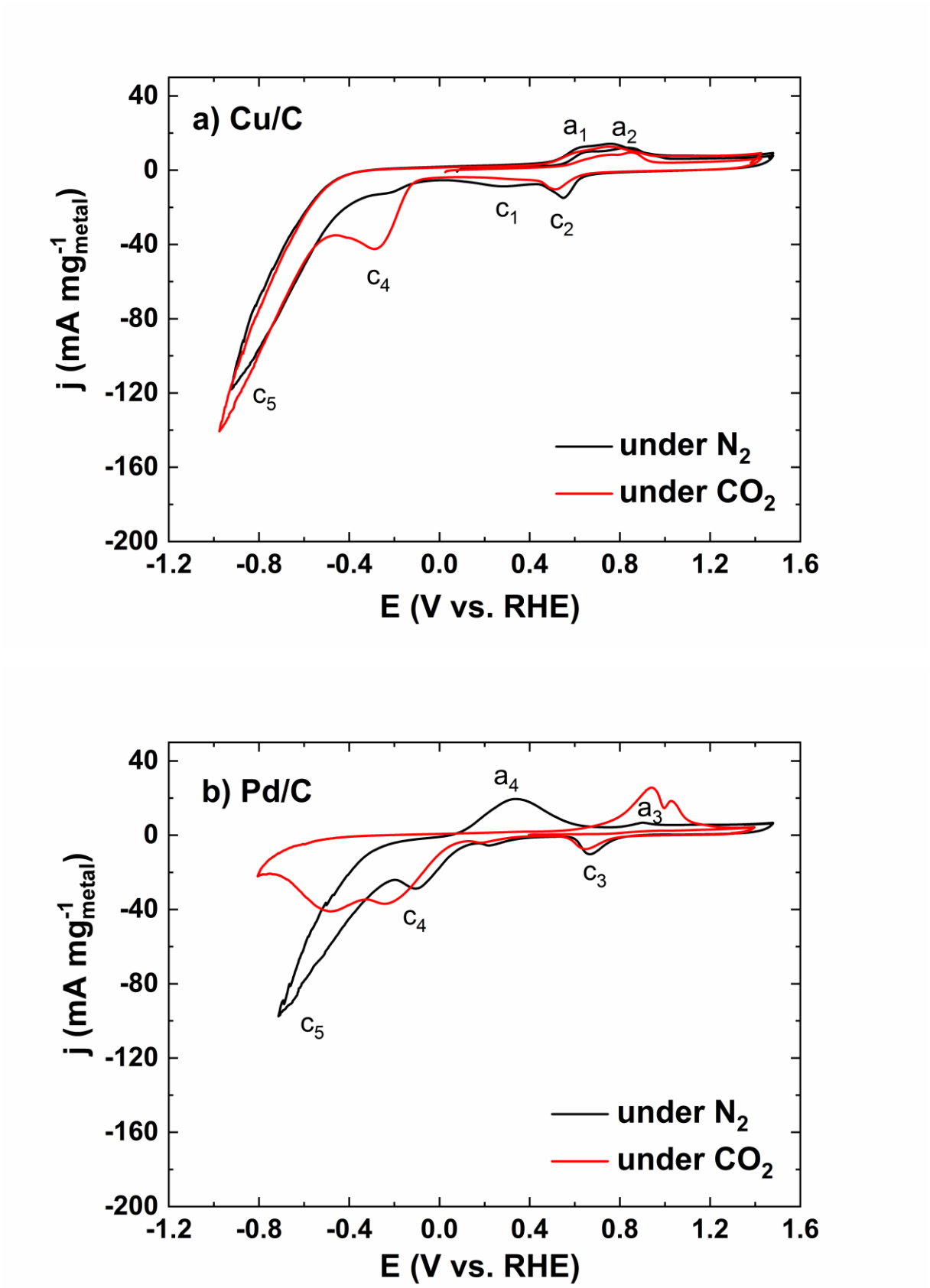

Figure S3. Cyclic voltammograms of the Cu/C (a) and Pd/C (b) electrodes recoded at 50 mV s^{-1} in a 0.5 mol L^{-1} $NaHCO_3$ electrolytic solution at 25 °C in the absence and presence of CO_2.

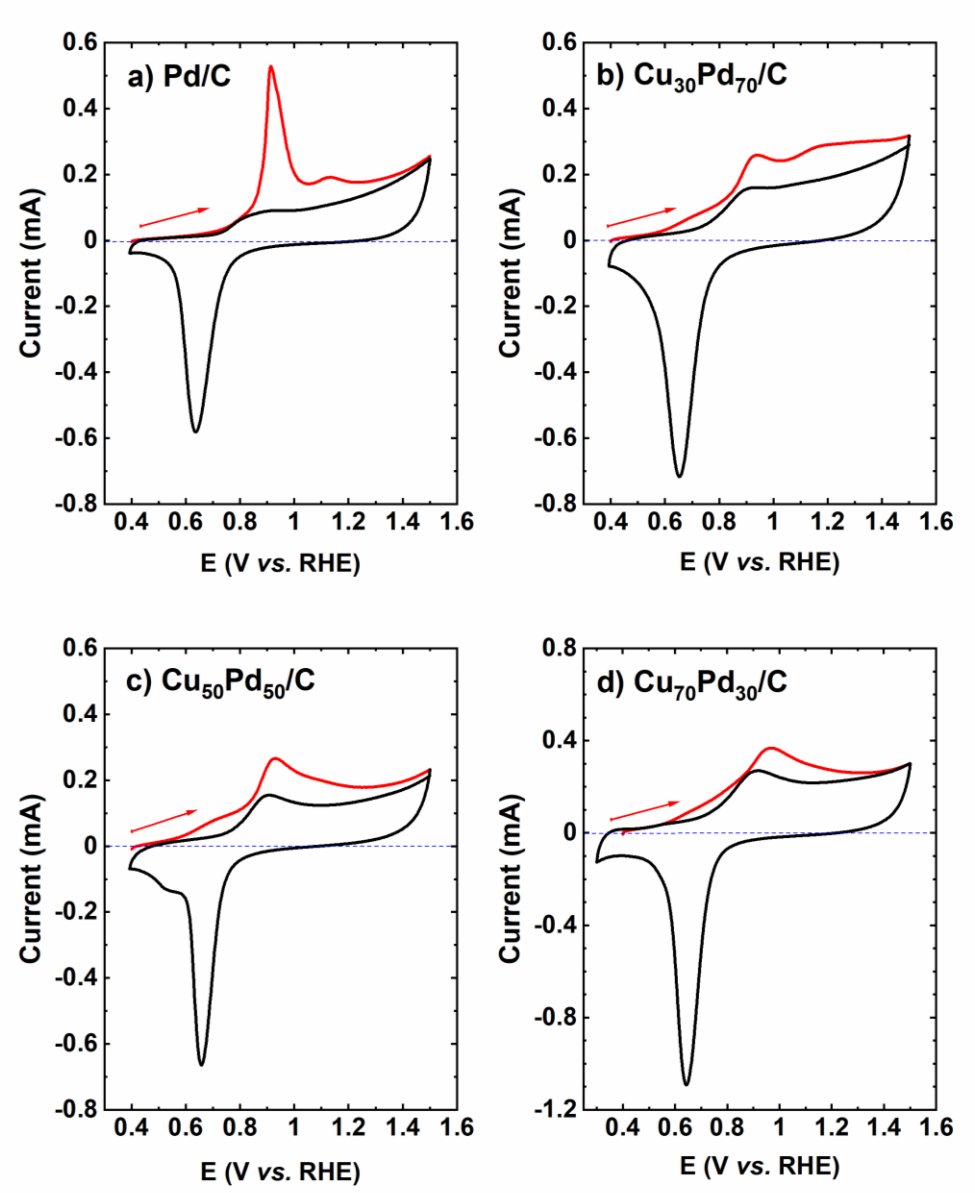

Figure S4. CO stripping voltammograms of the electrodes a) Pd/C b) $Cu_{30}Pd_{70}$/C c) $Cu_{50}Pd_{50}$/C and d) $Cu_{70}Pd_{30}$/C recoded at 20 mV s^{-1} in 0.5 mol L^{-1} $NaHCO_3$ electrolyte.

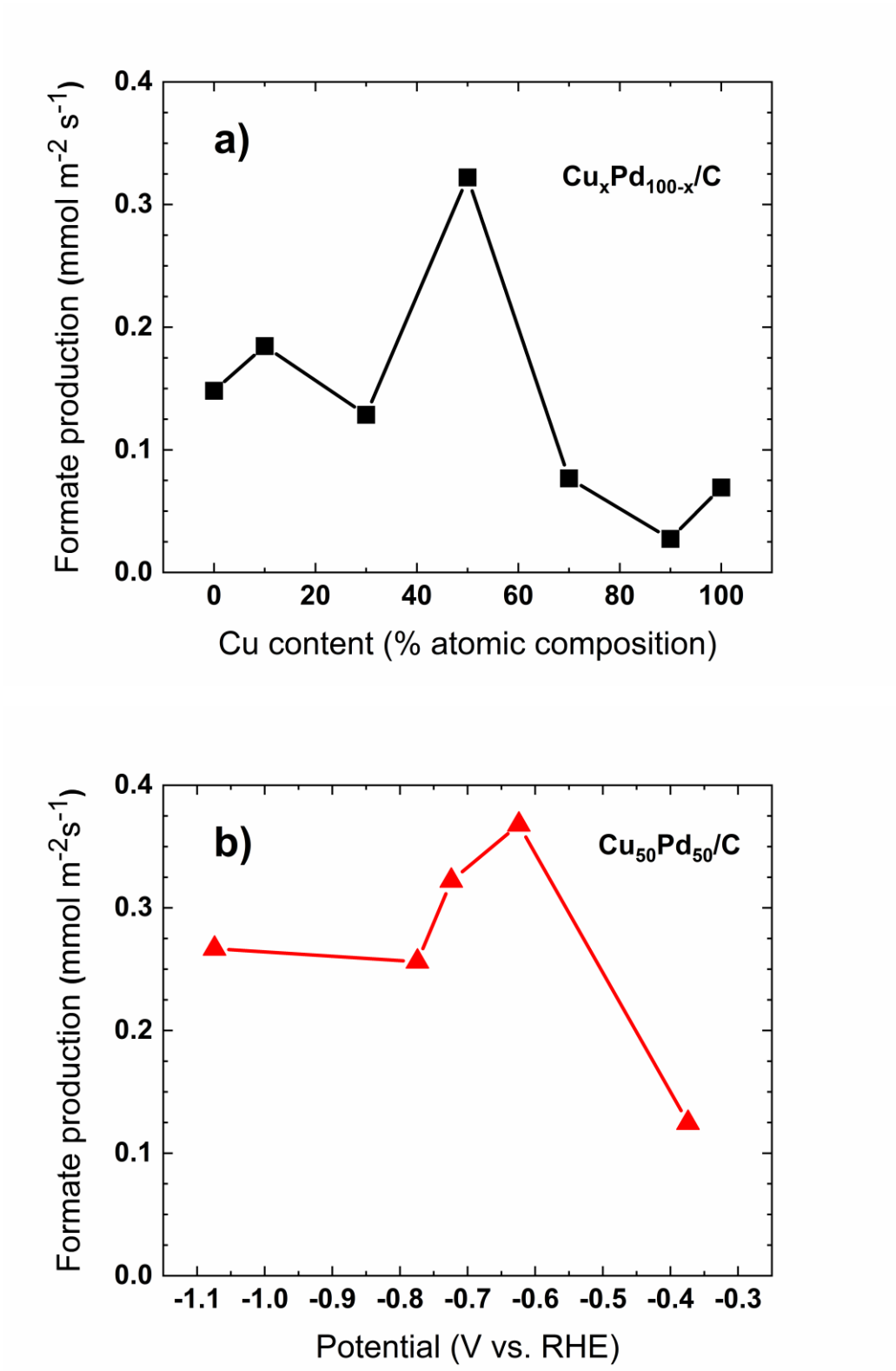

Figure S5. Production rates of formate (a) on the as-prepared Cu_xPd_{100-x}/C electrode materials at -0.72 V vs. RHE and (b) on $Cu_{50}Pd_{50}/C$ as function of the electrode potential.